International Journal of Biological Macromolecules 305 (2025) 140977

Contents lists available at ScienceDirect

International Journal of Biological Macromolecules

journal homepage: www.elsevier.com/locate/ijbiomac

Conformational heterogeneity and protonation equilibria shape the photocycle branching in channelrhodopsin-2

Luca Bellucci [a], Matteo Capone [b], Isabella Daidone [c], Laura Zanetti-Polzi [b,*]

[a] NEST-SNS, CNR Institute of Nanoscience, Piazza San Silvestro 12, Pisa 5612, Italy
[b] Center S3, CNR Institute of Nanoscience, Via Campi 213/A, Modena 41125, Italy
[c] Department of Physical and Chemical Sciences, University of L'Aquila, via Vetoio (Coppito 1), L'Aquila 67010, Italy

ARTICLE INFO

Keywords:
Photoactive proteins
Deprotonation free energy
Molecular dynamics

ABSTRACT

Channelrhodopsin-2 is a photoactive membrane protein serving as an ion channel, gathering significant interest for its applications in optogenetics. Despite extensive investigation, several aspects of its photocycle remain elusive and continue to be subjects of ongoing debate. Of particular interest are the localization of the P480 intermediate within the photocycle and the timing of the deprotonation of glutamic acid E90, a critical residue for ChR2 functioning. In this study, we explore the possibility of an early-P480 state, formed directly upon photoillumination of the dark-adapted state, where E90 is deprotonated, as hypothesized in a previous work [Kuhne et al. Proc. Natl. Acad. Sci. 116.19 (2019): 9380]. Employing extended molecular dynamics simulations, deprotonation free energy calculations, and the computation of the infrared band associated with E90, we provide support to the photocycle model proposed by Kuhne et al. Furthermore, our findings show that E90 protonation state is influenced by diverse interconnected variables and provide molecular detail insights that connect E90 interaction pattern with its deprotonation propensity. Our data demonstrate in fact that both protonated and deprotonated E90 are possible in P480 depending on E90 hydrogen bonding pattern and explaining the molecular mechanism at the basis of P480 accumulation under continuous illumination.

1. Introduction

Channelrhodopsins (ChRs) are membrane proteins belonging to the family of microbial rhodopsins that function as light-gated cation channels. The natural role of ChR is to serve as photoreceptors for phototaxis in green algae, where it is involved in the regulation of flagelar motion depending on lighting conditions, allowing the organism to seek light optimal for photosynthesis and survival [1]. In the past twenty years, ChRs have been widely applied in the emerging field of optogenetics that targets the optical control of neuronal cells to investigate their function. Channelrhodopsin-2 from *Chlamydomonas reinhardtii* (ChR2) is by far the most used optogenetic tool and the most investigated ChR [2]. As it is typical in microbial rhodopsins, in ChR2 the photoactive moiety is retinal, which is linked to a lysine residue, K257, through a protonated Schiff base. The protonated Schiff base is stabilized by two counterions, a glutamate (E123) and an aspartate (D253). Light exposure triggers retinal ultrafast isomerization from all-*trans* to 13-*cis*, initiating a sequence of conformational changes, the photocycle, that induce in ≈10 μs the opening of the internal channel switching the protein to the ion-conducting state. During the subsequent steps of the photocycle channel closing occurs and the dark-adapted state is ultimately recovered (see Fig. 1).

Despite the vast amount of work devoted to the investigation of ChR2 with a plethora of experimental and computational approaches, some key aspects of its photocycle are still unclear. One of the most controversial points arises from the fact that to rationalize all the experimental data, at least two closed states giving rise to an apparent dark state (D_{app}), along with a branched photocycle, are required (see Fig. 1) [2–8]. Yet, a consensus has not been reached nor on the characterization of the two closed states neither on the evolution of the hypothesized parallel photocycle. In addition, multiple isomerization states for the retinal have been proposed on the basis of infrared (IR), Raman and NMR spectroscopy: all-*trans*,C=N-*anti*; 13-*cis*,C=N-*anti*; 13-*cis*,C=N-*syn*; all-*trans*,C=N-*syn* [3,4,6,9,10]. Yet, these different isomers could not be unambiguously assigned to specific photocycle intermediates.

Interpretation of the experimental data is further complicated by the differing behavior of the system in single-turnover experiments and under continuous illumination. Under the latter conditions, alterations

* Corresponding author.
E-mail address: laura.zanettipolzi@nano.cnr.it (L. Zanetti-Polzi).

https://doi.org/10.1016/j.ijbiomac.2025.140977
Received 2 December 2024; Received in revised form 24 January 2025; Accepted 11 February 2025
Available online 14 February 2025

in ion selectivity, photocurrent inactivation, and a biexponential decay of the photocurrent are indeed observed [6]. The characterization of one photocycle intermediate, P480, is particularly puzzling. P480 is a long lived nonconductive state hypothesized to be a late intermediate, slowly decaying to the fully dark-adapted state D470 [5,11,12]. P480 was shown to accumulate under continuous illumination conditions [5,6] and it is thought to feature a 13-*cis*,C=N-*syn* retinal [6,7,12]. Some features of P480 make it a possible candidate for being the second closed state in the hypothetical branched photocycle: it was shown to be photoactive [5] and its spectral features are similar to those of the dark state [13,14]. In addition, the apparent dark-adapted state D_{app} was shown to include a mixture of all-*trans*,C=N-*anti* and 13-*cis*,C=N-*syn* isomers [4,9,15]. Furthermore, relaxation from the ion-conducting P520 intermediate to D470 bypassing P480 was observed [5] (see Fig. 1), making it difficult to incontrovertibly identify P480 as the last photocycle intermediate.

Another disputed point is the protonation state of a highly conserved glutamic acid, E90, along the photocycle. E90 is a crucial residue in ChR2 functioning [16]: it is part of the ion-conducting pore and an element of the central gate [17] and it is involved in ion selectivity. As a matter of fact, its mutation reduces the photocurrent [18] or even converts ChR2 into a chloride channel [19]. There is a general consensus on the fact that E90 is protonated in the fully dark adapted state and deprotonates along the photocycle. However, E90 deprotonation timing and role are still a subject of debate. In particular, both an early [16,18] and a late [20,21] deprotonation for this amino acid have been proposed. Interestingly, the late deprotonation was related to the late P480 intermediate [20].

In 2019 Kuhne et al. [6] proposed a new model of branched photocycle based on electrophysiology data, Raman and IR spectroscopy. According to their hypothesis, P480 is not the latest photocycle intermediate. On the contrary, it is the 13-*cis*,C=N-*syn* closed state found, together with D470, in the light adapted D_{app} state. Under continuous illuminations, both D470 and P480 are the starting points of two parallel photocycles with C=N-*anti* and C=N-*syn* retinal conformations respectively (see Fig. 1, black and magenta). The *anti* cycle evolves in the cation conducting state O1 (early and late, see Fig. 1, with different ion selectivity). The *syn* cycle, instead, evolves to the poorly conducting state O2 characterized by high proton selectivity (see Fig. 1, magenta). In addition, according to this model, E90 is protonated in the *anti* cycle and deprotonated in the *syn* cycle.

Despite the model proposed by Kuhne et al. appearing to reconcile most previous experimental observations, it was questioned in 2021 by the NMR data of Becker-Baldus et al. [7]. According to their interpretation, P480 cannot be directly formed after light excitation but, as previously proposed, it is instead a late intermediate in the photocycle appearing during channel closure. Their data suggest that P480 is photoactive, as proposed in the model of Kuhne et al., and termed its photoproduct P_x, proposing the photocycle model depicted in Fig. 1, black and green.

Here, we use large-scale molecular dynamics (MD) simulations and a hybrid quantum-classical approach to explore the thermodynamic feasibility of the early deprotonation of E90 in the 13-*cis*,C=N-*syn* closed state formed upon light excitation, i.e., in the early forming P480 state according to the photocycle model of Kuhne et al. We compute E90 deprotonation free energies in both D470 and P480 and we calculate the IR signal arising from E90 side chain, analyzing the sensitivity of the spectral signal to the conformational heterogeneity of the dark state. To these aims, we use a theoretical-computational approach based on the perturbed matrix method, the MD-PMM approach [22]. This strategy has already been used to model proton [23] and electron [24,25] transfer reactions and to calculate deprotonation free energies [26,27], and has been shown to accurately reproduce the experimentally measured pK_a differences among E/D residues embedded in the protein environment [26]. This approach is used here to investigate the protonation state of E90 in the early P480 state, which is obtained upon photoillumination of the D470 state, as it significantly impacts the evolution of the photocycle.

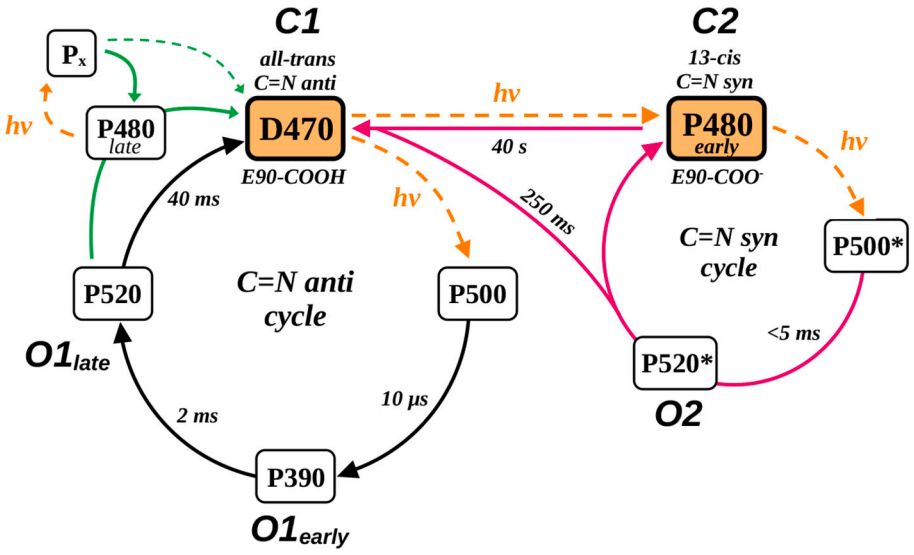

Fig. 1. Photocycle models proposed for ChR2. In the fully dark adapted state, D470, retinal is in the all-*trans*,C=N-*anti* isomer and E90 is protonated. Upon light illumination (dashed orange lines) ChR2 enters the main photocycle (in black) with an all-*trans*,C=N-*anti* → 13-*cis*,C=N-*anti* retinal isomerization reaching the P500 state. P500 then evolves to the two open states O1-early and O1-late with different ion selectivity. According to the model of Kuhne et al. [6], a second closed state C2 can be populated upon D470 photoillumination and is the P480 state (here called $P480_{early}$) in which retinal is in the 13-*cis*,C=N-*syn* isomer and E90 is deprotonated. Further photoexcitation of $P480_{early}$ induces a side photocycle (in magenta), that evolves to the highly proton selective and poorly conducting O2 state. In the photocycle model of Kuhne et al. [6] E90 stays protonated along the main (black) photocycle and deprotonated along the side (magenta) cycle. According to Becker-Baldus et al. [7], P480 cannot be reached directly from D470 but can be instead formed from P520 ($P480_{late}$, green cycle). Illumination of $P480_{late}$ leads to a new photoproduct termed P_x and characterized by a twisted retinal structure. Both $P480_{late}$ and P520 can relax back to D470. The two states investigated in the present work, D470 and $P480_{early}$, are highlighted in orange.

2. Results

2.1. Protonation state of E90 in D470

To investigate the protonation state of E90 in ChR2, we compute its deprotonation free energy using the MD-PMM approach (see section 4.2 and section 2 in the Supporting Information, SI). Initially, we compute the deprotonation free energy of a capped (i.e., N-terminal acetylated and C-terminal *N*-methyl amidated) glutamic acid (E) in solution to be used as reference for all subsequent calculations. Using the procedure presented in our previous work [26] and recalled in the SI, section 2.1, we estimate for capped-E a pK_a value of 3.9, in excellent agreement with the experimentally estimated pK_a of 4.3 in an alanine pentapeptide [28]. We then move to the estimate of the deprotonation free energy of E90 in D470, i.e. in the closed state C1 (see Fig. 1). To this aim we use two extended MD simulations (1.7 μs each) starting from the crystal structure of ChR2 [17]: one in the C1 state with all-*trans*,C=N-*anti* retinal and protonated E90 (anti-E90prot MD) and one in the C1 state with all-*trans*, C=N-*anti* retinal and deprotonated E90 (anti-E90dep MD). The latter is only required for obtaining the proper ensemble sampling necessary for the calculation of deprotonation free energies but is not representative of the D470 state (in which E90 is protonated, vide infra), thus will not be discussed in what follows. As anticipated on the basis of previous experimental evidences [13], we obtain that E90 is protonated in the D470 (anti) state: the deprotonation free energy of E90 is in fact 28 kJ/mol higher than that of capped-E in solution (see Fig. 2), corresponding to a pK_a value of 8.6. The agreement between the calculated pK_a value of E90 in D470 and the experimental evidence indicating that E90 is protonated in the D470 state, also serves as a benchmark for our approach in the context of the specific system under investigation. This validates both our methodology and the results obtained for states where no experimental indication is available.

Analysis of the anti-E90prot MD simulation shows that two hydrogen bonding (HB) patterns are possible for protonated E90 in the D470 state: a major conformational basin in which E90 is part of a tight HB network involving K93, E123, D253 and the protonated retinal Schiff base (PRSB) and a minor one in which E90 side chain is flipped and hydrogen bonded to N258 (see Fig. 3 a1 and a2). Since in the first HB pattern E90 points towards the extracellular side and in the second towards the cytoplasmic side, we will refer in what follows to these two HB pattern as DOWN-253 and UP-258, respectively. A more detailed characterization of the HB pattern of E90 in D470 is reported in the SI, Fig. S5, showing that the UP-258 pattern is populated in ≈10% of the total sampled configurations, i.e., it is rather minor. In a previous simulation [29], the UP-258 pattern has been reported as stable HB interaction for E90 (approximately 60 % of a 300 ns-long MD simulation). In a different work, only the DOWN-253 pattern was observed in 5 parallel 100-ns long MD simulations [6]. Along our anti-E90prot MD, we observe some partial flips and one reversible transition from DOWN-253 to UP-258, in which the UP-258 HB pattern remains stable for ≈200 ns. Such timescale is consistent with both previous findings. Notably, E90 was observed in the UP-258 pattern also in the previously obtained crystal structure of the ChR1/ChR2 (C1C2) chimera in the closed D470 state [30] and was shown to be stable for hundreds of ns along MD simulations starting from that crystal structures [31,32].

2.2. Deprotonation propensity of E90 in the early P480 state

In the scenario proposed by Kuhne et al. [6], early formation of P480 occurs upon photoexcitation of D470 inducing, in parallel with the conventional all-*trans*,C=N-*anti* → 13-*cis*,C=N-*anti* isomerization, also the all-*trans*,C=N-*anti* → 13-*cis*,C=N-*syn* isomerization. To investigate

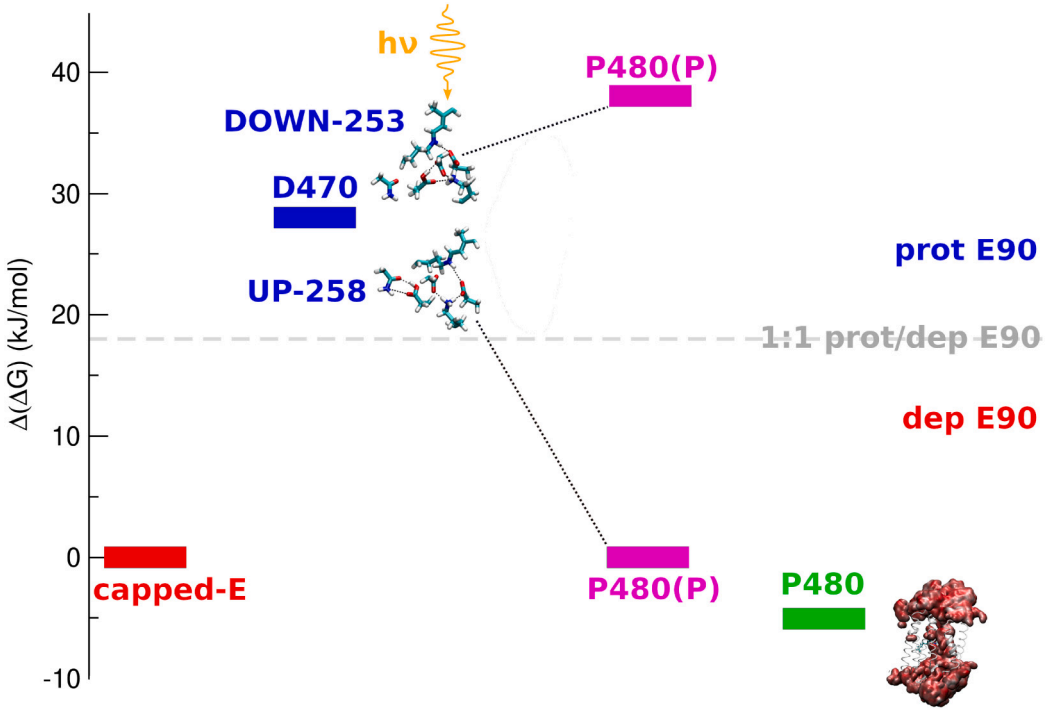

Fig. 2. Schematics of E90 deprotonation free energies as obtained by the present calculations. All deprotonation free energies are reported as the difference Δ(ΔG) with respect to the deprotonation free energy of capped-E. For Δ(ΔG) values below/above ≈18 kJ/mol deprotonated/protonated E90 is favored. The standard error for Δ(ΔG) values, estimated through the standard error of their mean ($\sigma/\sqrt{n}$) calculated over *n* subtrajectories, is ≈ 8 kJ/mol. In the D470 state (all-*trans*,C=N-*anti* retinal, in blue) E90 is protonated and can be found in both the DOWN-253 and UP-258 HB patterns. Upon light illumination the all-*trans*,C=N-*anti* → 13-*cis*,C=N-*syn* isomerization occurs leading to the P480(P) state, with protonated E90 (magenta). If the photoisomerization occurs from the DOWN-253 pattern the free energy value is such that E90 stays protonated. On the contrary, if the photoisomerization occurs from the UP-258 pattern the free energy value is such that E90 gets deprotonated. Once the proton is lost, the P480 state with deprotonated E90 (green) is stabilized by the rupture of the K93-D253 HB and subsequent access of water in the protein interior.

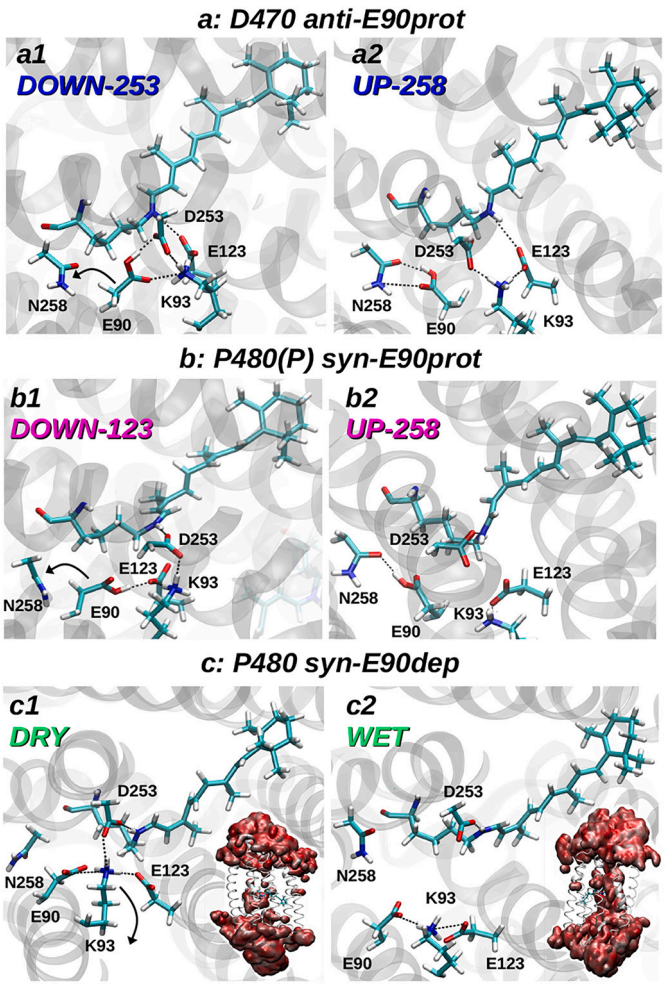

Fig. 3. Representative snapshots of the HB patterns sampled along the MD simulations in the D470 and P480 states. In the D470 state (panel a) two HB patterns are observed. In the DOWN-253 pattern (panel a1) E90 interacts with D253 and K93; in the UP-258 pattern (panel a2) E90 interacts with N258. Along the MD simulation in the P480 state with E90 protonated (P480(P), panel b), for starting structures in the DOWN-253 pattern there is a switch to the DOWN-123 pattern, where E90 mainly interacts with E123 (panel b1) while for starting structures in the UP-258 pattern the interaction is maintained (panel b2). Along the MD simulation in the P480 state with E90 deprotonated (P480, panel c), two HB patterns are observed. In both of them E90 interacts with K93. In the first one (panel c1) K93 also interacts with D253 and E123. In the second one (panel c2), the K93-D253 interaction is not present, determining an "opening" in the retinal cavity that enhances the access of water in the protein interior, as shown in the bottom structures where water is represented as a red surface.

the E90 protonation thermodynamics in what is hypothesized to be the early P480 state, we simulated the so-called C2 state with 13-*cis*,C=N-*syn* retinal and protonated E90 (namely *syn*-E90prot MD). This is required to calculate the propensity of E90 to undergo deprotonation in the 13-*cis*,C=N-*syn* photo-product isomer generated from the D470 ensemble. Therefore, we extracted from the anti-E90prot MD simulations 10 configurations of the whole system in such a way that one monomer is found in the DOWN-253 HB pattern and the other in the UP-258 HB pattern. From these configurations we generate 10 starting configurations for 10 *syn*-E90prot MD simulations (40 ns length each, see section 4.1 and 1.1 in the SI for the details on the isomerization process). This procedure creates by design *syn*-E90prot configurations in which E90 is both in the UP-258 and in the DOWN-253 HB pattern, thus assuming that the all-*trans*,C=N-*anti* to 13-*cis*,C=N-*syn* isomerization is possible for both conformers. This assumption can be validated by combining available experimental data. In fact, the apparent dark-adapted state D_{app} was shown to include a mixture of all-*trans*,C=N-*anti* and 13-*cis*,C=N-*syn* isomers both in ChR2 and in the C1C2 chimera [4,9,15]. In addition, in the crystal structure of ChR2 E90 is downward oriented while in the crystal structure of the C1C2 chimera E90 is in the UP-258 conformer. Taken together, these data suggest that the all-*trans*, C=N-*anti* to 13-*cis*,C=N-*syn* isomerization is possible in both the UP and the DOWN HB pattern. Inspection of the 10 *syn*-E90prot MDs shows that, in the monomer starting from the UP-258 configurations, the E90-N258 interaction is maintained along all ten 40 ns-long MDs. Instead, in the monomer starting from the DOWN-253 configurations, the all-*trans*, C=N-*anti* → 13-*cis*,C=N-*syn* isomerization determines a different HB pattern inside the retinal binding pocket (Fig. 3b and Fig. S5). In fact, E90 HB partner changes from D253 to E123 after ≈15 ns (on average) of the *syn*-E90prot MDs. In what follows, we will refer to the E90-E123 interaction as DOWN-123 pattern.

To pursue a more in-depth analysis of the conformational ensemble sampled of the *syn*-E90prot state and to the sensitivity of the MD simulations to the initial conditions we perform an additional extended (1.7 μs) *syn*-E90prot MD simulation starting from the crystal structure with 13-*cis*,C=N-*syn* retinal. As a matter of fact, in the crystal structure both all-*trans*,C=N-*anti* and 13-*cis*,C=N-*syn* isomers can be accommodated without perturbing the structure of the retinal pocket [17]. Analysis of the extended syn-E90prot simulation shows that, upon isomerization, the E90 HB pattern change observed in the parallel shorter *syn*-E90prot MDs is reproduced: already during the equilibration runs we observe the formation of the E90-E123 HB, that remains then stable for the rest of the simulation. Note that in the crystal structure E90 is not hydrogen bonded to either D253 or E123, with a similar O—O distance of ≈4.5–5 Å. Therefore, E90 preferential interaction with D253 in the anti-E90prot MD and with E123 in the *syn*-E90prot MD are determined by the different interactions resulting from the distinct isomerization state. We also observe that along the extended syn-E90prot MD the UP-258 pattern is never spontaneously formed. The results obtained in the 10 short and in the extended MD, taken together, suggest that the possibility of having the UP-258 pattern in the syn-E90prot state is determined by the conformational ensemble of the D470 state.

The above point is particularly relevant when moving to the calculation of E90 deprotonation free energy in the syn-E90prot state. In fact, the calculation of deprotonation free energies provides rather different results for the DOWN-123 and UP-258 patterns. E90 deprotonation results to be highly discouraged in the DOWN-123 pattern: the deprotonation free energy is even higher than that obtained in the D470 state by ≈10 kJ/mol (see Fig. 2). This can be rationalized analyzing E90 interactions in the anti-E90prot and *syn*-E90prot states (i.e., DOWN-253 and DOWN-123 pattern, respectively). In both states, E90 interacts with a negatively charged carboxylic sidechain, strongly discouraging deprotonation. However, in the anti-E90prot MD the interaction with the positively charged K93 partially mitigates the above effect. In the syn-E90dep MD K93 is on average farther, further disfavoring E90 deprotonation (see Figure 3a1 and b1 and Fig. S5 in the SI).

Interestingly, E90 deprotonation is instead possible in the UP-258 pattern, in which the deprotonation free energy results to be as low as that of capped-E in solution (see Fig. 2). The UP-258 HB pattern, that is only sampled in the D470 state, promotes therefore deprotonation of E90, showing that the conformational variability of the dark *anti* state is crucial for the deprotonation step in the *syn* state. It is important to highlight that the deprotonation of E90 in the P480 state requires the deprotonation step to be faster than the transition from the UP conformation to the DOWN conformation. Nonetheless, the thermodynamic feasibility of the deprotonation step is supported by the observation that, during all 10 syn-E90 protonated 40 ns-long MD simulations, no UP to DOWN transition is observed, along with experimental evidence indicating that E90 deprotonation occurs relatively quickly (estimated to be faster than 1 ns, as the E90-deprotonation marker band appears instantaneously and is not time-resolved) [6].

Deprotonation of E90 in the UP-258 HB pattern is a viable route also

from the perspective of the proton transport pathway. In fact, in the UP-258 pattern, besides being hydrogen-bonded to N258, E90 is also hydrogen-bonded to a water molecule, with an average occupancy of ≈90% across the ten 40 ns-long trajectories. Visual inspection of the trajectories shows that in most MD frames there is a chain of hydrogen bonded water molecules, sometimes also including specific protein residues that can serve as proton shuttles, that connects E90 sidechain to bulk water at either the intra- or the extracellular side (representative snapshots are provided in Fig. S6 in the SI). Using a graph-theory [33] based approach and following the same strategy we previously employed for the investigation of bulk water [34], we build a network associated to each configuration sampled along the ten 40-ns long trajectories starting from the UP-258 conformer and we calculate in this graph the paths connecting E90 sidechain to bulk water (see Section 1.2 in the SI). This analysis is performed over all MD frames of 10 independent trajectories, generating a distribution of paths and ensuring the statistical robustness of the results. The analysis shows that the average fraction of frames in which at least one path is present is 0.86± 0.06 and that, on average, the shortest path from E90 to bulk water involves 7.1 ± 2.5 edges. Interestingly, in a non-negligible fraction of frames (0.26 ± 0.06) the calculated shortest paths involve histidine (H) 134. This residue is part of the so-called inner gate (H134-E83) and was previously suggested to be part of a biological "proton wire" involved in proton conductance [1].

2.3. Stabilization of deprotonated E90 in the early P480 state

To assure that E90 is deprotonated in the early P480 state, the thermodynamic feasibility of the deprotonation step in the *syn*-E90prot state is not sufficient and must be coupled to a stabilization of the syn-E90dep state. We therefore complete our analysis with the investigation of the syn-E90dep state. To this aim we perform an extended (2.0 μs) MD using as starting point the crystal structure with 13-*cis*,C=N-*syn* retinal and deprotonated E90. Along the MD trajectory, we observe a major conformational change. While in the first part the residues in the retinal binding pocket are bound in a tight HB network with E90 forming a strong salt bridge with K93 (Figure 3c1, DRY conformation), at ≈ 1.2 μs this HB network is partially disrupted (see also Figs. S5 and S7a in the SI). In particular, rupture of the HB between K93 and D253 occurs and induces the two transmembrane helices TM2 and TM7 to move away one from the other (Figure 3c2, WET conformation). This leads to a considerable increase of water in the interior of the protein, as shown in Fig. S7 in the SI, consistently with what observed in previous MDs [6]. Calculation of E90 deprotonation free energy in the *syn*-E90dep state reveals that this conformational change strongly stabilizes deprotonated E90. In fact, as predictable, water influx and increased hydration of the retinal binding cavity strongly stabilizes E90 deprotonated state, leading to a deprotonation free energy that is even lower than that of capped-E by ≈5 kJ/mol (see Fig. 2). As a very relevant point, we observe the rupture of the K93-D253 interaction in most of our ten syn-E90prot MD simulations starting in the UP-258 HB pattern. As a matter of fact, as shown in Fig. S7b in the SI, the K93-D253 HB remains stable only in three trajectories, while in the other seven trajectories it starts breaking at ≈10 ns and is not present for ≈60% of the MD. This suggests that loss of the proton in the P480(P) state occurs in a conformation that is already prone to undergo the conformational change we observe in the extended syn-E90dep MD and leading to the stabilization of deprotonated E90. It is also important to emphasize that the DRY to WET conformational change is triggered by the combined effects of E90 deprotonation and all-*trans*,C=N-*anti* to 13-*cis*,C=N-*syn* isomerization. In fact, the anti-E90 deprotonated MD (i.e., the MD in the D470 state with deprotonated E90) does not exhibit any rupture of the retinal binding pocket hydrogen bond network or any water influx into the protein interior (see Fig. S8 in the SI).

2.4. Calculation of E90 IR absorption bands in D470

Since our data point to a crucial role of E90 HB interactions in the dark state, we explore the possibility of experimentally distinguishing between the D470 DOWN-253 and UP-258 patterns. To this aim, we calculate the IR absorption band due to E90 side chain using the MD-PMM approach. The MD-PMM has been already utilized for calculating C=O stretching IR bands, both from the backbone [35] and from aspartate side chains [36]. A specific application for rhodopsins has already been achieved [37]. Here, we compute the signal arising from protonated E90 sidechain C=O stretching in D470, separating the signal arising from the DOWN-253 pattern from that arising from the UP-258 pattern (details on the IR spectra calculation are provided in the SI, section 2.2). Interestingly, the calculated spectra (Fig. 4) show that the two HB patterns provide different IR signals. As a matter of fact, the frequency peak corresponding to the UP-258 HB pattern, i.e. 1735 cm^{-1} is upshifted by 16 cm^{-1} with respect to that corresponding to the DOWN-253 HB pattern, i.e. 1719 cm^{-1}. The observed frequency upshift is in accordance with the HB weakening that accompanies the DOWN to UP transition. Remarkably, in a previous experimental work [20] two bands, at 1728 cm^{-1} and at 1717 cm^{-1}, were assigned to two distinct HB patterns of E90. The experimentally observed frequency upshift (11 cm^{-1}) very well agrees with the computed shift between the DOWN and UP conformers (16 cm^{-1}) and the absolute values of the two computed frequencies also well match the corresponding experimental values (1719 cm^{-1} calc. vs 1717cm^{-1} exp. and 1735 cm^{-1} calc. vs 1728 cm^{-1} exp.). Since we do not shift any of our calculated frequencies to match the corresponding experimental frequency (see section 2B in the SI for more details), the comparison of both the frequency shift and the absolute frequencies is meaningful. The good agreement between the calculated and experimental signals suggests a close correspondence between the underlying E90 structures and HB patterns. This is particularly relevant because the experimentally observed 11 cm^{-1} upshift was suggested to result from a change in E90 HB pattern that precedes E90 deprotonation. This provides strong support to the conclusions drawn by our deprotonation free energy data: a transition from the DOWN-253 (at lower frequencies) to the UP-258 (at higher frequencies) HB patterns has to occur prior to deprotonation.

3. Discussion and conclusion

Using extended MD simulations (7.5 μs in total) and deprotonation

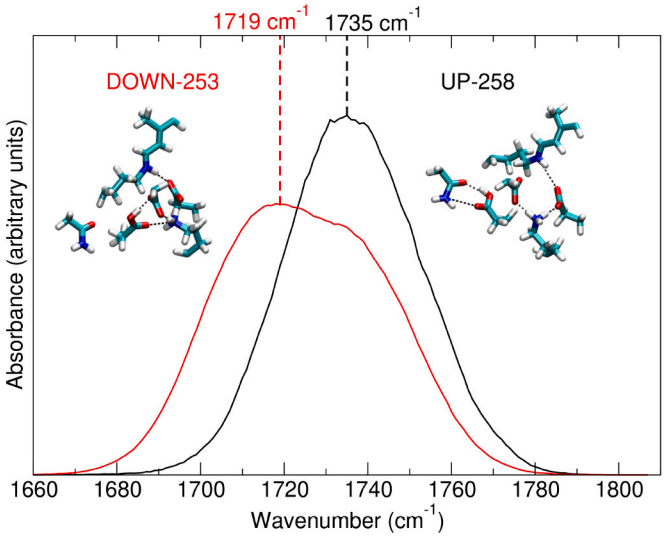

Fig. 4. Calculated IR spectra for the two different HB patterns of E90 in the D470 state. Black: UP-258 pattern; red: DOWN-253 pattern.

free energy calculations we investigate the protonation state of E90 in the early P480 that can be obtained upon photoillumination of the D470 state, as hypothesized in the work of Kuhne et al. [6]. According to our results, both protonated and deprotonated E90 are possible in P480. Specifically, our calculations show that if the all-*trans*,C=N-*anti* → 13-*cis*,C=N-*syn* isomerization (i.e., D470 → P480) takes place within D470 major conformational basin in which a HB between E90 and D253 is formed (DOWN-253 pattern) E90 remains protonated in the P480 state. On the contrary, if the isomerization occurs in the minor conformational basin in which a HB between E90 and N258 is formed (UP-253 pattern), deprotonation of E90 can occur. Based on the experimental evidence that E90 is deprotonated along the side cycle [6], we suggest that only this latter minor population progresses from P480 into the side cycle. The remaining population, which retains a protonated E90, does not enter the side cycle and accounts for P480 accumulation. The emerging picture nicely agrees, and further completes, the photocycle model proposed by Kuhne et al. [6] as it explains the microscopic origin of P480 accumulation observed in their Raman experiments under continuous illumination (or at high flash frequency).

Identification of the mechanism underlying the deprotonation propensity of E90 can guide mutagenesis studies aimed at optimizing optogenetic tools based on the use of ChR2. Specifically, mutations that favor the UP-258 HB pattern and, consequently, E90 deprotonation may produce a more efficient cycle unaffected by the accumulation of the P480 state. One possible mutation in this direction could be the substitution of Asn with Asp at position 258. This mutation was already studied in the C1C2 chimera [31] and was shown to strengthen the 90–258 interaction without inhibiting the photocycle.

Our results also reconcile the IR data of Kuhne et al. [6] with the previous IR data of Lórenz-Fonfría et al. [20], who concluded, on the basis of an upshift of E90 IR band, that E90 changes its HB pattern before deprotonation. In their work, the signal upshift was interpreted as corresponding to a weakening of the E90-N258 interaction due to retinal isomerization. Yet, at that time only the crystal structure of the C1C2 chimera, in which E90 is hydrogen bonded to N258, was available. The calculations we perform here of E90 side chain IR bands show that the experimentally observed frequency upshift upon deprotonation can be ascribed to the change from the DOWN-253 (tighter HB) to the UP-258 (weaker HB) E90 conformation that, according to our free energy calculations, is required for E90 deprotonation. Notably, this is in accordance with the observation of Lórenz-Fonfría et al. that the IR frequency upshift precedes E90 deprotonation. Therefore, our results explain the origin of E90 IR band upshift observed by Lórenz-Fonfría et al. in the context of the early P480 state proposed by Kuhne et al. [6].

In addition, our calculations provide evidence that in ChR2 the intrinsic conformational heterogeneity of the dark state plays a major role in the photocycle evolution. The dark state heterogeneity was already proposed to be essential in determining the early stages of rhodopsins photocycle [38,39], also showing that complex excited-state relaxation behaviors mainly arise from the acid-base equilibrium of the Schiff base counterions [40]. Our data not only support this picture, showing that the protonation/deprotonation equilibria of crucial residues in the dark state can strongly affect the photocycle evolution, but also show that the protonation state of these residues is itself tuned by the conformational heterogeneity of the dark state.

We emphasize that in the present work we focus exclusively on D470 and P480-early, and therefore we cannot provide information about events occurring at latest stages of the photocycle. We also acknowledge the intrinsic limitations of classical MD simulations, including finite sampling, the use of fixed protonation states, and the fully classical representation of hydrogen atoms. The latter approximation is also relevant in free energy calculations, where the effects of delocalized electron density on the sidechain group of E90 due to hydrogen bonding are neglected. Nonetheless, the classical treatment of E90's hydrogen bond partners enables us to exploit the main strength of the MD-PMM approach, namely the inclusion of conformational heterogeneity in large complex systems by utilizing the extended sampling provided by classical MD simulations to calculate free energies and spectral signals. In fact, the possibility to explore different conformational basins of D470 allows us to rationalize the molecular mechanisms underlying E90 deprotonation.

In summary, our results support the hypothesis proposed by Kuhne et al. [6] regarding the existence of an early P480 state formed upon photoillumination of D470, initiating a side cycle in which E90 is deprotonated. Our findings further expand on this picture by demonstrating that multiple protonation states are possible for E90 in the closed state: depending on its HB pattern, E90 can either remain protonated, leading to P480 accumulation, or become deprotonated, allowing progression from P480 into the side cycle. We show that the protonation/deprotonation equilibrium of E90 in the 13-*cis*,C=N-*syn* photoilluminated P480 state is strongly influenced by the intrinsic conformational heterogeneity of the all-*trans*,C=N-*anti* dark state D470. According to our results, the protonation state of E90 in the closed state is governed by several interconnected factors, and its deprotonation is a cooperative process requiring: i) all-*trans*,C=N-*anti* → 13-*cis*,C=N-*syn* retinal isomerization, ii) a specific hydrogen bonding HB pattern of E90 in D470, and iii) water influx into the protein interior.

4. Methods

4.1. MD simulations set-up

We perform in the present paper MD simulations in four different states of ChR2: 1) D470 anti-E90prot state, with all-*trans*,C=N-*anti* retinal and protonated E90; 2) D470(D) anti-E90dep state, with all-*trans*, C=N-*anti* retinal and deprotonated E90; 3) P480(P) *syn*-E90prot state, with 13-*cis*,C=N-*syn* retinal and protonated E90; 4) P480 syn-E90dep state, with 13-*cis*,C=N-*syn* retinal and deprotonated E90. The D470(D) simulation (2) is required only for the computation of the absolute value of E90 deprotonation free energy and corresponding pK_a value. As a matter of fact, it is known that E90 is protonated in the D470 state. For all states we perform a 1.7 μs-long MD simulation (with the exception of MD 4 that is 2 μs long to achieve a better sampling after the DRY to WET transition) starting from the crystal structure of ChR2 (PDB ID 6EID, Fig. S1), that well accommodates both the all-*trans*,C=N-*anti* and the 13-*cis*,C=N-*syn* retinal isomers [17]. A detailed schematic representation of all the MD simulations is provided in Fig. S2.

In line with previous MD simulations of ChR2 [6,41,42], standard protonation states are used for all residues with the exception of E90, for which different protonation states are tested as above outlined, and D156 that is modeled as protonated as it has been recognized as the proton donor to the Schiff base in the subsequent steps of the photocycle [6]. In particular, the two Schiff base counterions, i.e. E123 and D253, are modeled as deprotonated in both the *anti* and the *syn* simulations. As a matter of fact, both residues have been suggested to act as proton acceptors of the PRSB during the photocycle [16,20] and the crystal structure [17] shows that the all-*trans*,C=N-*anti* to 13-*cis*,C=N-*syn* isomerization results in a minor change in the position of the RSB proton, preserving the salt bridge between the PRSB and the counterion complex. Besides the four extended MD simulations performed in the four different states, we perform 10 additional 40 ns-long MD simulations in the P480(P) *syn*-E90prot state using as starting structures 10 configurations randomly extracted from the D470 anti-E90 state MD portion of trajectory in which one monomer is in the DOWN-253 HB pattern and the other monomer is in the UP-258 HB pattern (see Fig. 3). For these 10 simulations retinal all-*trans*,C=N-*anti* → 13-*cis*,C=N-*syn* retinal double isomerization was performed using steered molecular dynamics (SMD). MD simulations are performed with the NAMD2.13 suite [43,44] using the CHARMM36 force field [45–47] to treat all interactions and the TIP3P model for water [48]. A similar computational protocol was already successfully employed in previous MD simulations of complex membrane systems [49–51]. Additional information on the

MD simulations, including SMDs, are provided in section 1, Table S1, and in Figs. S1-S4 of the SI. The initial structures for the D470 anti-E90prot and P480 syn-E90dep MD simulations are provided as Supplementary Material available for download. Additional data are available upon request from the authors.

4.2. The MD-PMM approach

The MD-PMM approach [22], like other hybrid quantum/classical methodologies [52–54], is based on partitioning the system under investigation into two regions: (1) the quantum center (QC), which contains atoms associated with the processes of interest (e.g., protonation/deprotonation events or molecular vibrations) and is treated at the quantum level, and (2) the rest of the system (the environment), which influences the properties of the QC via an electrostatic perturbation obtained from the system's atomistic classical MD configurations. The main strength of the MD-PMM is that the perturbed properties of the QC can be evaluated using a considerable number of atomistic configurations of the environment obtained from extended classical MD simulations of the whole system (including the quantum part). As a matter of fact, in the MD-PMM the perturbation operator is expanded so that the presence of the environment is applied *a posteriori* onto the quantum properties of the QC. The quantum properties of the QC (i.e. the unperturbed properties) are obtained with quantum mechanical calculations in the gas phase (see section 3 in the SI). Then, for each configuration/frame generated by all-atoms classical MD simulations, the QC Hamiltonian operator is perturbed by the instantaneous electrostatic field resulting from the environment's instantaneous configuration. The electronic Hamiltonian operator $\widehat{H}_k$ of the QC embedded in the perturbing environment of configuration k is thus:

$$\widehat{H}_k = \widehat{H}^0 + \widehat{V}_k \tag{1}$$

where $\widehat{H}^0$ is the QC unperturbed Hamiltonian obtained considering the isolated QC and $\widehat{V}_k$ is the perturbation operator from environment configuration k. In constructing the perturbed Hamiltonian matrix, the diagonal elements are obtained by expanding the perturbation operator around each individual atom of the QC while for the nondiagonal elements the perturbing electric field provided by the environment's atomic charges is used to determine the perturbation operator via a multipolar expansion centered on the QC's center of mass, $\mathbf{r_0}$. Therefore, the elements $V_{i,j}$ between the electronic states i and j can be expressed as:

$$V_{i,j} \approx \delta_{i,j}\sum_N \mathscr{V}(\mathbf{R}_N)q_{N,i} - \left(\mathbf{E}(\mathbf{r}_0)\cdot\boldsymbol{\mu}_{i,j}\right)\left(1-\delta_{i,j}\right) \tag{2}$$

with N running over all QC atoms. $\mathbf{R}_N$ is the N*th* QC nucleus position, $q_{N,i}$ is the corresponding atomic charge in the state i, $\mathscr{V}$ is the electrostatic potential exerted by the perturbing environment, $\mathbf{E}$ is the perturbing electric field ($\mathbf{E} = -\partial\mathscr{V}/\partial\mathbf{r}$), $\boldsymbol{\mu}_{i,j}$ is the QC transition dipole moment, and $\delta_{i,j}$ is the Kronecker delta. At each frame of the MD simulation ensemble (i.e., for each configuration k of the environment), the perturbed electronic Hamiltonian matrix is constructed and diagonalized, providing a continuous trajectory of perturbed eigenvalues and eigenvectors. The QC's instantaneous perturbed quantum observable of interest can be then evaluated for each environment configuration. In the present case, we are interested in computing the deprotonation free energy and sidechain vibrational band of protonated E90. Therefore, we select as QC acetate and acetic acid to compute the perturbed energy change upon deprotonation (see Eqs. 1–5 in the SI) and acetate to compute the C═O stretching frequency in E90 sidechain. More details are provided in the SI, sections 2 and 3, as well as in the original works [26,36].

CRediT authorship contribution statement

Luca Bellucci: Writing – review & editing, Writing – original draft, Investigation, Formal analysis, Conceptualization. **Matteo Capone:** Writing – review & editing, Investigation, Formal analysis. **Isabella Daidone:** Writing – review & editing, Formal analysis. **Laura Zanetti-Polzi:** Writing – review & editing, Writing – original draft, Investigation, Formal analysis, Conceptualization.

Declaration of competing interest

The authors declare that they have no known competing financial interests or personal relationships that could have appeared to influence the work reported in this paper.

Acknowledgments

M.C. and L.Z.P. acknowledge funding from MUR through PRIN 2022-WS44W4-EnvELOP. The authors thank Valeria Giliberti, Eleonora Temperini and Stefano Corni for fruitful discussion and helpful comments.

Appendix A. Supplementary data

Additional details on molecular dynamics simulations (including steered molecular dynamics); details on the calculation of the proton transfer pathway; application of the MD-PMM approach for the calculation of deprotonation free energies and for the calculation of carboxylic sidechains infrared spectra; details on quantum mechanical calculations; list of abbreviations and their definitions; sketch of the MDs starting structure; schematics of the MD simulation protocol; RMSD of the protein backbone along the simulations; sketch of the retinal isomers; hydrogen bonding interactions along the MD simulations; representative snapshot of hydrogen bond chains connecting E90 side chain to bulk water; retinal binding pocket structural change in P480; E90 hydration in P480 and D470-E90dep; initial structures for the D470 anti-E90prot and P480 *syn*-E90dep MD simulations. Supplementary data to this article can be found online at https://doi.org/10.1016/j.ijbiomac.2025.140977.

References

[1] K. Deisseroth, P. Hegemann, The form and function of channelrhodopsin, Science 357 (6356) (2017) eaan5544.
[2] F. Schneider, C. Grimm, P. Hegemann, Biophysics of channelrhodopsin, Annu. Rev. Biophys. 44 (2015) 167–186.
[3] J. Becker-Baldus, C. Bamann, K. Saxena, H. Gustmann, L.J. Brown, R.C. Brown, C. Reiter, E. Bamberg, J. Wachtveitl, H. Schwalbe, et al., Enlightening the photoactive site of channelrhodopsin-2 by dnp-enhanced solid-state nmr spectroscopy, Proc. Natl. Acad. Sci. 112 (32) (2015) 9896–9901.
[4] S. Bruun, D. Stoeppler, A. Keidel, U. Kuhlmann, M. Luck, A. Diehl, M.-A. Geiger, D. Woodmansee, D. Trauner, P. Hegemann, et al., Light–dark adaptation of channelrhodopsin involves photoconversion between the all-trans and 13-cis retinal isomers, Biochemistry 54 (35) (2015) 5389–5400.
[5] M. Saita, F. Pranga-Sellnau, T. Resler, R. Schlesinger, J. Heberle, V.A. Lorenz-Fonfria, Photoexcitation of the p4480 state induces a secondary photocycle that potentially desensitizes channelrhodopsin-2, J. Am. Chem. Soc. 140 (31) (2018) 9899–9903.
[6] J. Kuhne, J. Vierock, S.A. Tennigkeit, M.-A. Dreier, J. Wietek, D. Petersen, K. Gavriljuk, S.F. El-Mashtoly, P. Hegemann, K. Gerwert, Unifying photocycle model for light adaptation and temporal evolution of cation conductance in channelrhodopsin-2, Proc. Natl. Acad. Sci. 116 (19) (2019) 9380–9389.
[7] J. Becker-Baldus, A. Leeder, L.J. Brown, R.C. Brown, C. Bamann, C. Glaubitz, The desensitized channelrhodopsin-2 photointermediate contains 13-cis, 15-syn retinal schiff base, Angew. Chem. 133 (30) (2021) 16578–16583.
[8] R. Polito, M.E. Temperini, E. Ritter, L. Puskar, U. Schade, M. Broser, P. Hegemann, L. Baldassarre, M. Ortolani, V. Giliberti, Conformational changes of a membrane protein determined by infrared difference spectroscopy beyond the diffraction limit, Phys. Rev. Appl. 16 (1) (2021) 014048.
[9] M. Nack, I. Radu, C. Bamann, E. Bamberg, J. Heberle, The retinal structure of channelrhodopsin-2 assessed by resonance raman spectroscopy, FEBS Lett. 583 (22) (2009) 3676–3680.

[10] E. Ritter, P. Piwowarski, P. Hegemann, F.J. Bartl, Light-dark adaptation of channelrhodopsin c128t mutant, J. Biol. Chem. 288 (15) (2013) 10451–10458.
[11] M.-K. Verhoefen, C. Bamann, R. Blöcher, U. Förster, E. Bamberg, J. Wachtveitl, The photocycle of channelrhodopsin-2: ultrafast reaction dynamics and subsequent reaction steps, ChemPhysChem 11 (14) (2010) 3113–3122.
[12] V.A. Lórenz-Fonfría, B.-J. Schultz, T. Resler, R. Schlesinger, C. Bamann, E. Bamberg, J. Heberle, Pre-gating conformational changes in the cheta variant of channelrhodopsin-2 monitored by nanosecond ir spectroscopy, J. Am. Chem. Soc. 137 (5) (2015) 1850–1861.
[13] E. Ritter, K. Stehfest, A. Berndt, P. Hegemann, F.J. Bartl, Monitoring light-induced structural changes of channelrhodopsin-2 by uv-visible and fourier transform infrared spectroscopy, J. Biol. Chem. 283 (50) (2008) 35033–35041.
[14] M. Nack, I. Radu, B.-J. Schultz, T. Resler, R. Schlesinger, A.-N. Bondar, C. del Val, S. Abbruzzetti, C. Viappiani, C. Bamann, et al., Kinetics of proton release and uptake by channelrhodopsin-2, FEBS Lett. 586 (9) (2012) 1344–1348.
[15] V. Muders, S. Kerruth, V.A. Lórenz-Fonfría, C. Bamann, J. Heberle, R. Schlesinger, Resonance raman and ftir spectroscopic characterization of the closed and open states of channelrhodopsin-1, FEBS Lett. 588 (14) (2014) 2301–2306.
[16] J. Kuhne, K. Eisenhauer, E. Ritter, P. Hegemann, K. Gerwert, F. Bartl, Early formation of the ion-conducting pore in channelrhodopsin-2, Angew. Chem. Int. Ed. 54 (16) (2015) 4953–4957.
[17] O. Volkov, K. Kovalev, V. Polovinkin, V. Borshchevskiy, C. Bamann, R. Astashkin, E. Marin, A. Popov, T. Balandin, D. Willbold, et al., Structural insights into ion conduction by channelrhodopsin 2, Science 358 (6366) (2017) eaan8862.
[18] K. Eisenhauer, J. Kuhne, E. Ritter, A. Berndt, S. Wolf, E. Freier, F. Bartl, P. Hegemann, K. Gerwert, In channelrhodopsin-2 glu-90 is crucial for ion selectivity and is deprotonated during the photocycle, J. Biol. Chem. 287 (9) (2012) 6904–6911.
[19] J. Wietek, J.S. Wiegert, N. Adeishvili, F. Schneider, H. Watanabe, S.P. Tsunoda, A. Vogt, M. Elstner, T.G. Oertner, P. Hegemann, Conversion of channelrhodopsin into a light-gated chloride channel, Science 344 (6182) (2014) 409–412.
[20] V.A. Lórenz-Fonfría, T. Resler, N. Krause, M. Nack, M. Gossing, G. Fischer von Mollard, C. Bamann, E. Bamberg, R. Schlesinger, J. Heberle, Transient protonation changes in channelrhodopsin-2 and their relevance to channel gating, Proc. Natl. Acad. Sci. 110 (14) (2013) E1273–E1281.
[21] T. Resler, B.-J. Schultz, V.A. Lórenz-Fonfría, R. Schlesinger, J. Heberle, Kinetic and vibrational isotope effects of proton transfer reactions in channelrhodopsin-2, Biophys. J. 109 (2) (2015) 287–297.
[22] L. Zanetti-Polzi, S. Del Galdo, I. Daidone, M. D'Abramo, V. Barone, M. Aschi, A. Amadei, Extending the perturbed matrix method beyond the dipolar approximation: comparison of different levels of theory, Phys. Chem. Chem. Phys. 20 (37) (2018) 24369–24378.
[23] L. Zanetti-Polzi, M.D. Smith, C. Chipot, J.C. Gumbart, D.L. Lynch, A. Pavlova, J. C. Smith, I. Daidone, Tuning proton transfer thermodynamics in sars-cov-2 main protease: implications for catalysis and inhibitor design, J. Phys. Chem. Lett. 12 (17) (2021) 4195–4202.
[24] M. Capone, A. Sirohiwal, M. Aschi, D.A. Pantazis, I. Daidone, Alternative fast and slow primary charge-separation pathways in photosystem ii, Angew. Chem. 135 (16) (2023) e202216276.
[25] M. Capone, G. Dell'Orletta, B.T. Nicholls, G.D. Scholes, T.K. Hyster, M. Aschi, I. Daidone, Evidence of a distinctive enantioselective binding mode for the photoinduced radical cyclization of α-chloroamides in ene-reductases, ACS Catal. 13 (23) (2023) 15310–15321.
[26] L. Zanetti-Polzi, I. Daidone, A. Amadei, Fully atomistic multiscale approach for p k a prediction, J. Phys. Chem. B 124 (23) (2020) 4712–4722.
[27] L. Zanetti-Polzi, P. Charchar, I. Yarovsky, S. Corni, Origins of the ph-responsive photoluminescence of peptide-functionalized Au nanoclusters, ACS Nano 16 (12) (2022) 20129–20140.
[28] G.R. Grimsley, J.M. Scholtz, C.N. Pace, A summary of the measured pk values of the ionizable groups in folded proteins, Protein Sci. 18 (1) (2009) 247–251.
[29] W. Zhang, T. Yang, S. Zhou, J. Cheng, S. Yuan, G.V. Lo, Y. Dou, Molecular dynamics simulation of transmembrane transport of chloride ions in mutants of channelrhodopsin, Biomolecules 9 (12) (2019) 852.
[30] H.E. Kato, F. Zhang, O. Yizhar, C. Ramakrishnan, T. Nishizawa, K. Hirata, J. Ito, Y. Aita, T. Tsukazaki, S. Hayashi, et al., Crystal structure of the channelrhodopsin light-gated cation channel, Nature 482 (7385) (2012) 369–374.
[31] M.R. VanGordon, L.A. Prignano, R.E. Dempski, S.W. Rick, S.B. Rempe, Channelrhodopsin c1c2: Photocycle kinetics and interactions near the central gate, Biophys. J. 120 (9) (2021) 1835–1845.
[32] C. Cheng, M. Kamiya, M. Takemoto, R. Ishitani, O. Nureki, N. Yoshida, S. Hayashi, An atomistic model of a precursor state of light-induced channel opening of channelrhodopsin, Biophys. J. 115 (7) (2018) 1281–1291.
[33] A.C. Patel, S. Sinha, G. Palermo, Graph theory approaches for molecular dynamics simulations, Q. Rev. Biophys. 57 (2024) e15.
[34] C. Faccio, N. Di Fonte, I. Daidone, L. Zanetti-Polzi, Enhanced connectivity and mobility in liquid water: implications for the high density liquid structure and its onset, J. Mol. Liq. 392 (2023) 123425.
[35] C.M. Davis, L. Zanetti-Polzi, M. Gruebele, A. Amadei, R.B. Dyer, I. Daidone, A quantitative connection of experimental and simulated folding landscapes by vibrational spectroscopy, Chem. Sci. 9 (48) (2018) 9002–9011.
[36] S.M.V. Pinto, N. Tasinato, V. Barone, A. Amadei, L. Zanetti-Polzi, I. Daidone, Modeling amino-acid side chain infrared spectra: the case of carboxylic residues, Phys. Chem. Chem. Phys. 22 (5) (2020) 3008–3016.
[37] V. Giliberti, R. Polito, E. Ritter, M. Broser, P. Hegemann, L. Puskar, U. Schade, L. Zanetti-Polzi, I. Daidone, S. Corni, et al., Tip-enhanced infrared difference-nanospectroscopy of the proton pump activity of bacteriorhodopsin in single purple membrane patches, Nano Lett. 19 (5) (2019) 3104–3114.
[38] Y. Guo, F.E. Wolff, I. Schapiro, M. Elstner, M. Marazzi, Different hydrogen bonding environments of the retinal protonated schiff base control the photoisomerization in channelrhodopsin-2, Phys. Chem. Chem. Phys. 20 (43) (2018) 27501–27509.
[39] J.F. Bada Juarez, P.J. Judge, S. Adam, D. Axford, J. Vinals, J. Birch, T.O. Kwan, K. K. Hoi, H.-Y. Yen, A. Vial, et al., Structures of the archaerhodopsin-3 transporter reveal that disordering of internal water networks underpins receptor sensitization, nature, Communications 12 (1) (2021) 629.
[40] C.-F. Chang, H. Kuramochi, M. Singh, R. Abe-Yoshizumi, T. Tsukuda, H. Kandori, T. Tahara, A unified view on varied ultrafast dynamics of the primary process in microbial rhodopsins, Angew. Chem. Int. Ed. 61 (2) (2022) e202111930.
[41] Y. Guo, F.E. Beyle, B.M. Bold, H.C. Watanabe, A. Koslowski, W. Thiel, P. Hegemann, M. Marazzi, M. Elstner, Active site structure and absorption spectrum of channelrhodopsin-2 wild-type and c128t mutant, Chem. Sci. 7 (6) (2016) 3879–3891.
[42] A. Ardevol, G. Hummer, Retinal isomerization and water-pore formation in channelrhodopsin-2, Proc. Natl. Acad. Sci. 115 (14) (2018) 3557–3562.
[43] J.C. Phillips, D.J. Hardy, J.D.C. Maia, J.E. Stone, J.V. Ribeiro, R.C. Bernardi, R. Buch, G. Fiorin, J. Hénin, W. Jiang, R. McGreevy, M.C.R. Melo, B.K. Radak, R. D. Skeel, A. Singharoy, Y. Wang, B. Roux, A. Aksimentiev, Z. Luthey-Schulten, L. V. Kalé, K. Schulten, C. Chipot, E. Tajkhorshid, Scalable molecular dynamics on CPU and GPU architectures with NAMD, J. Chem. Phys. 153 (4) (2020) 044130.
[44] J.E. Stone, J.C. Phillips, P.L. Freddolino, D.J. Hardy, L.G. Trabuco, K. Schulten, Accelerating molecular modeling applications with graphics processors, J. Comput. Chem. 28 (16) (2007) 2618–2640.
[45] R.B. Best, X. Zhu, J. Shim, P.E. Lopes, J. Mittal, M. Feig, A.D. MacKerell Jr., Optimization of the additive charmm all-atom protein force field targeting improved sampling of the backbone ϕ, ψ and side-chain χ1 and χ2 dihedral angles, J. Chem. Theory Comput. 8 (9) (2012) 3257–3273.
[46] J. Huang, A.D. MacKerell Jr., Charmm36 all-atom additive protein force field: validation based on comparison to nmr data, J. Comput. Chem. 34 (25) (2013) 2135–2145.
[47] S. Jo, T. Kim, V.G. Iyer, W. Im, Charmm-gui: a web-based graphical user interface for charmm, J. Comput. Chem. 29 (11) (2008) 1859–1865.
[48] A.D. MacKerell Jr., D. Bashford, M. Bellott, R.L. Dunbrack Jr., J.D. Evanseck, M. J. Field, S. Fischer, J. Gao, H. Guo, S. Ha, et al., All-atom empirical potential for molecular modeling and dynamics studies of proteins, J. Phys. Chem. B 102 (18) (1998) 3586–3616.
[49] A. Felline, L. Bellucci, V. Vezzi, C. Ambrosio, S. Cotecchia, F. Fanelli, Structural plasticity of arrestin-g protein coupled receptor complexes as a molecular determinant of signaling, Int. J. Biol. Macromol. 137217 (2024).
[50] L. Bellucci, A. Felline, F. Fanelli, Dynamics and structural communication in the ternary complex of fully phosphorylated v2 vasopressin receptor, vasopressin, and -arrestin 1, Biochim. Biophys. Acta Biomembr. 1862 9 (2020) 183355.
[51] N. Varma, E. Mutt, J. Mühle, V. Panneels, A. erakita, X. Deupi, P. Nogly, G. F. Schertler, E. Lesca, Crystal structure of jumping spider rhodopsin-1 as a light sensitive gpcr, Proceedings of the National Academy of Sciences 116 (29) (2019) 14547–14556.
[52] H.M. Senn, W. Thiel, Qm/mm methods for biomolecular systems, Angew. Chem. Int. Ed. 48 (7) (2009) 1198–1229.
[53] B. Mennucci, S. Corni, Multiscale modelling of photoinduced processes in composite systems, Nat. Rev. Chem. 3 (5) (2019) 315–330.
[54] M.-A. Mroginski, S. Adam, G.S. Amoyal, A. Barnoy, A.-N. Bondar, V.A. Borin, J. R. Church, T. Domratcheva, B. Ensing, F. Fanelli, et al., Frontiers in multiscale modeling of photoreceptor proteins, Photochem. Photobiol. 97 (2) (2021) 243–269.